Angewandte Chemie

Supporting Information

Observation of the Low-Frequency Spectrum of the Water Dimer as a Sensitive Test of the Water Dimer Potential and Dipole Moment Surfaces

Raffael Schwan, Chen Qu, Devendra Mani, Nitish Pal, Lex van der Meer, Britta Redlich, Claude Leforestier, Joel M. Bowman,* Gerhard Schwaab, and Martina Havenith*

anie_201906048_sm_miscellaneous_information.pdf

1 Methods

1.1 Helium Nanodroplet Isolation (HeNDI) Spectroscopy

The design of our helium nanodroplet isolation spectrometer has been descibed recently. [1, 2, 3] Since many review articles on performing spectroscopy in helium droplets have already been published, [4, 5, 6, 7, 8] only a brief summary is given here.

The helium nanodroplet isolation spectrometer consists of four vacuum chambers (*i.e.* the expansion chamber, the pickup chamber, the spectroscopy chamber, and the detection chamber), which are differentially pumped and interconnected using conflat flanges.

In the expansion chamber, helium droplets are generated by a continuous expansion of pre-cooled, highly pressurized, ultrapure ^{4}He gas (99.9999 % purity) through a nozzle with $5\,\mu$m diameter into vacuum. For the present study, the nozzle is maintained at 18 K and the backing pressure is 40 bar. The generated helium droplets are further collimated using a skimmer of 0.5 mm diameter. The helium droplets further cool down through evaporative cooling, until they attain their equilibrium temperature of 0.37 K.

The collimated helium droplet beam enters the pickup chamber, where dopant molecules are added. In the present study, small amounts of water are added from an external reservoir to the chamber *via* a dosing valve. For spatially confined pickup regions, it is well established that the pickup of molecules by the droplets follows Poisson statistics. The probability of a pickup of k (dopant molecules) by a helium droplet is given by:

$$P_k = \frac{(\sigma l \rho)^k}{k!} \exp(\sigma l \rho), \tag{1}$$

where ρ is the number density directly proportional to its partial pressure of the dopant molecule in the pickup chamber, σ is the cross-section of the helium droplet and l is the length of the pickup region. By controlling the partial pressure of the dopant molecule inside the pickup chamber, the pickup of the dopant molecules by the helium droplets can be controlled. The thermal energy of the dopant molecules rapidly dissipates by evaporation of helium atoms from the droplet and they quickly equilibrate back to the temperature of 0.37 K, with a typical cooling rate of 10^{10} K/s. [6]

The free-electron lasers, FEL-I and FEL-II, at the FELIX laboratory produce radiation in the frequency region of $66 - 3600\,\mathrm{cm}^{-1}$. The operating principle and technical details of these lasers are summarized elsewhere. [9] Only some specific features of the FELIX radiation are discussed here. The FELIX radiation consists of macropulses of ~5−8 μs duration, with a repetition rate of 10 Hz. Each macropulse consists of a train of several thousand bandwidth-limited micropulses of a few ps duration, spaced by ~1 ns. The energy for each micropulse is up to 20 μJ and for each macropulse up to 80 mJ. The spectral bandwidth of each macropulse can be adjusted in the range of $0.2 - 5$ % of the central frequency. For the frequency region of $70-550\,\mathrm{cm}^{-1}$, covered in the present study, the spectral bandwidth was optimized to $0.2 - 0.4$ % of the central frequency.

In the spectroscopy chamber, the FELIX beam is aligned antiparallel and collinear to the helium droplet beam. Undoped helium droplets are transparent

to the IR radiation. However, in the case of doped helium droplets, the embedded molecule can absorb IR radiation. During the subsequent relaxation, the energy is transferred to the helium droplets, which results in the evaporation of helium atoms (*i.e.* in the depletion of the helium droplets). Each evaporated helium atom accounts for approximately 5 cm^{-1}. [10] In helium droplets, the relaxation process takes place at a nanosecond timescale. [8] Hence, excited molecules will relax between the micropulses and, therefore, a molecule can be excited multiple times within the duration of a single macropulse.

In the detection chamber, the helium droplets are ionized by electron impact ionization. This chamber hosts a quadrupole mass spectrometer (Extrel QMS MAX-1000), which is used to monitor the ion current of a certain fragment as a function of time. Any evaporation of helium atoms reduces the ionization cross-section of the helium droplets and, thus, decreases the measured ion current.

1.2 Twelve-dimensional (6d+6d) vibrational calculations

The methods used to calculate the VRT and FIR/THz spectra have been described in full details previously, [11, 12] and are briefly recalled below. The twelve-dimensional (12d) dimer system can be formally considered as made of two subsystems, weakly coupled in the energy range considered here: i) the "fast" intramolecular coordinates $\mathbf{q}^A$ and $\mathbf{q}^B$ associated to the monomer's vibrations; ii) the "slow" intermolecular ones $\mathbf{Q} = (R, \mathbf{\Omega}^A, \mathbf{\Omega}^B)$ describing the relative position and orientations of these monomers. The modes of interest in this study only originate from these later coordinates.

The calculations first proceed by defining, from the WHBB water potential, [13] an adiabatic dimer potential $V_{ad}(\mathbf{Q})$ as the lowest solution, at fixed $\mathbf{Q}$, of the 6d intramolecular ($\mathbf{q}^A$, $\mathbf{q}^B$) subsystem. This approximation is justified by the large energy separation between the two subsystems. Then, a correct description of the intermolecular subsystem $\mathbf{Q}$ requires to resort to a collisional formulation [14] as the Euler angles $\mathbf{\Omega}^A$ and $\mathbf{\Omega}^B$ experience large amplitude motions.

For a given J rotational quantum number value VRT levels are obtained, within each irreducible representation Γ_i of the G_{16} permutation-inversion (molecular symmetry) group, [15] by the direct Lanczos iterative method [16] which avoids explicitly building the corresponding Hamiltonian matrix. Only the recursive application of the Hamiltonian operator $\hat{H}_{\text{inter}}$ on some initial random vector $|u_0\rangle$ is required. One advantage of this method is that energy levels converge by increasing values in this case as the VRT levels, within a given Γ_i, correspond to the less dense part of the spectrum.

The FIR/THz spectrum $\alpha(\bar{\nu}, T)$ at temperature T is calculated in the usual way, as the Boltzmann average over state-to-state transitions $\mathbf{n}'' \rightarrow \mathbf{n}'$, the composite index $\mathbf{n}$ standing for the set $(vKJM\Gamma)$ of quantum numbers,

$$\alpha(\bar{\nu}, T) = \left\{ \sum_{\mathbf{n}''} \sum_{\mathbf{n}' > \mathbf{n}''} I_{\mathbf{n}' \leftarrow \mathbf{n}''} \cdot \mathcal{L}(\bar{\nu}, \bar{\nu}_t, \gamma) \right\} \times L \frac{T_0}{T} p_{WD} \quad,$$
$$\bar{\nu}_t = \frac{1}{hc}(E_{\mathbf{n}'} - E_{\mathbf{n}''}) \tag{2}$$

using a van Vleck-Weisskopf line shape function $\mathcal{L}$, and L is the Loschmidt's constant. $\mathbf{n}' > \mathbf{n}''$ means that the sum is restricted to levels $\mathbf{n}'$ lying above level

$\mathbf{n}''$ as the stimulated emission is already accounted for by the term $P_{\mathbf{n}''} - P_{\mathbf{n}'}$ in the expression below

$$I_{\mathbf{n}' \leftarrow \mathbf{n}''} = \frac{8\pi^3 \overline{\nu}_t}{4\pi\epsilon_0 3hc} \cdot (P_{\mathbf{n}''} - P_{\mathbf{n}'}) \cdot S_{\mathbf{n}' \leftarrow \mathbf{n}''} \quad ,$$

$$S_{\mathbf{n}' \leftarrow \mathbf{n}''} = 3 \sum_M \left| \left\langle \Psi_{v'}^{J'M\Gamma'} \left| \mu_Z^{SF} \right| \Psi_{v''K''}^{J''M\Gamma''} \right\rangle \right|^2 \tag{3}$$

The calculations are for 4 K and so all significantly populated initial J states were included in the calculations. It should be noted that for the low-lying populated energy states $\mathbf{n}''$ at temperature $0.37\,\mathrm{K}$, K'' can be considered as a good quantum number as the water dimer is a near prolate symmetrical top. This assumption is no longer valid for the final states $\Psi_{v'}^{J'M\Gamma'}$ reached as the spectrum covers the range $\overline{\nu} \in [0, 600]\,\mathrm{cm}^{-1}$. It results in basis set sizes of the order of $2 \times 10^5 \times (2J'+1)$, which are very efficiently handled within a Lanczos scheme: in that case, the initial recursion vector is defined by $|u_0\rangle = \mu_Z^{SF} \left| \Psi_{v''K''}^{J''M\Gamma''} \right\rangle$. Scott and Wyatt [17] showed how one can directly get the residues $\langle \Psi_{\mathbf{n}'} | u_0 \rangle$, *i.e.* the projections of the eigenstates $\Psi_{\mathbf{n}'}$ onto the initial Lanczos vetor u_0, without actually computing the eigenstates *per se*. In the calculations of the rovibrational line strength factors $S_{\mathbf{n}' \leftarrow \mathbf{n}''}$, the following selection rules apply: $\Gamma_i^+ \leftrightarrow \Gamma_i^-, \Delta J = 0, \pm 1$.

1.3   Quasiclassical Molecular Dynamics (QCMD)

The IR spectra of water dimer in the region from 0 to $600\,\mathrm{cm}^{-1}$ were calculated using a QCMD approach to obtain the dipole-dipole autocorrelation function, the Fourier transform of which provides the IR spectrum.

In QCMD simulations, zero-point energy is given initially to each normal mode of the molecule. This approach is widely used in reaction dynamics, where it is referred to as the quasiclassical approach, and so we use that terminology here. This is an approximate semiclassical quantization procedure and thus energy transfer between modes can occur, so this approach suffers from the "zero-point energy leak". The energy migration from high frequency intramolecular modes to low-frequency intermolecular ones can result in rapid dissociation of the dimer. To mitigate this rapid dissociation, we apply the approximate semiclassical quantization to intermolecular modes only and give zero energy initially to the intramolecular modes.

We used normal-mode sampling, described in Ref. [18], to prepare the initial conditions of the trajectories. As mentioned above, zero-point energy was assigned to all the intermolecular modes, but we did not put any energy in other intramolecular modes. The total angular momentum was set to zero. Five hundred QCMD trajectories were run to obtain the spectrum. Each trajectory was integrated for 24 ps, and the step size is 0.024 fs, using the velocity-Verlet algorithm. The potential energies and forces were calculated using the WHBB water potential, [19] which includes one accurate monomer potential [20] and an intrinsic two-body one. [21] The dipole moment of the instantaneous configuration was calculated every ten steps using the dipole moment surface that consists of an accurate monomer component developed by Lodi *et al.* [22] and an intrinsic two-body dipole developed by us. [23, 24] The dipole-dipole autocorrelation function was calculated as $C(t) = \langle \boldsymbol{\mu}(t) \cdot \boldsymbol{\mu}(0) \rangle$, where the brackets

indicate an ensemble average over 500 trajectories of the same total energy. Then $C(t)$ was Fourier transformed to obtain the IR spectra.

1.4 Pressure-dependent intensity measurements

As discussed above, it is well established that the pickup of molecules by helium droplets follows Poisson statistics. The probability of a pickup of k dopant molecules by a helium droplet is given by equation 1.

Hence, when recording the signal intensity at a certain frequency while varying the dopant partial pressure (*i.e.* by taking a pickup curve), the underlying cluster size of the signal can be determined. Normalization is achieved by plotting the signal intensity as a function of the product $\sigma l \rho$.

In the present study, for each signal with significant IR intensity, a pickup curve was recorded. In particular, pickup curves were obtained at the following frequencies: 86, 99, 115, 185, 283, 296, 492, and 503 cm^{-1} (see Figure 1). Since most signals were found to correspond to more than one water cluster size, an extended model was used that takes into account contributions from two different values k_1 and k_2:

$$P_{k_1,k_2} = a_1 \frac{(\sigma l \rho)^{k_1}}{k_1!} \exp(\sigma l \rho) + a_2 \frac{(\sigma l \rho)^{k_2}}{k_2!} \exp(\sigma l \rho) \quad , \tag{4}$$

where a_1 and a_2 are the amplitudes of the individual contributions of the Poisson statistics with k_1 and k_2, respectively.

2 Vibration-Rotational Tunneling (VRT) energy diagram for the low frequency intermolecular modes

By comparison to previous gas phase studies, the absorption bands in the frequency range from 70 to 145 cm^{-1} in our HENDI study could be assigned to transitions to the Donor Torsion (DT), Acceptor Wag (AW), and Acceptor Twist (AT) mode. In the following, we display for each of these modes an energy diagram including all experimentally observed transitions in the gas phase as well as the transitions observed our study, see Figure 2, 3, and 4, respectively. All states which are expected to be populated, assuming a Boltzmann population at 0.37 K, are shown as solid lines.
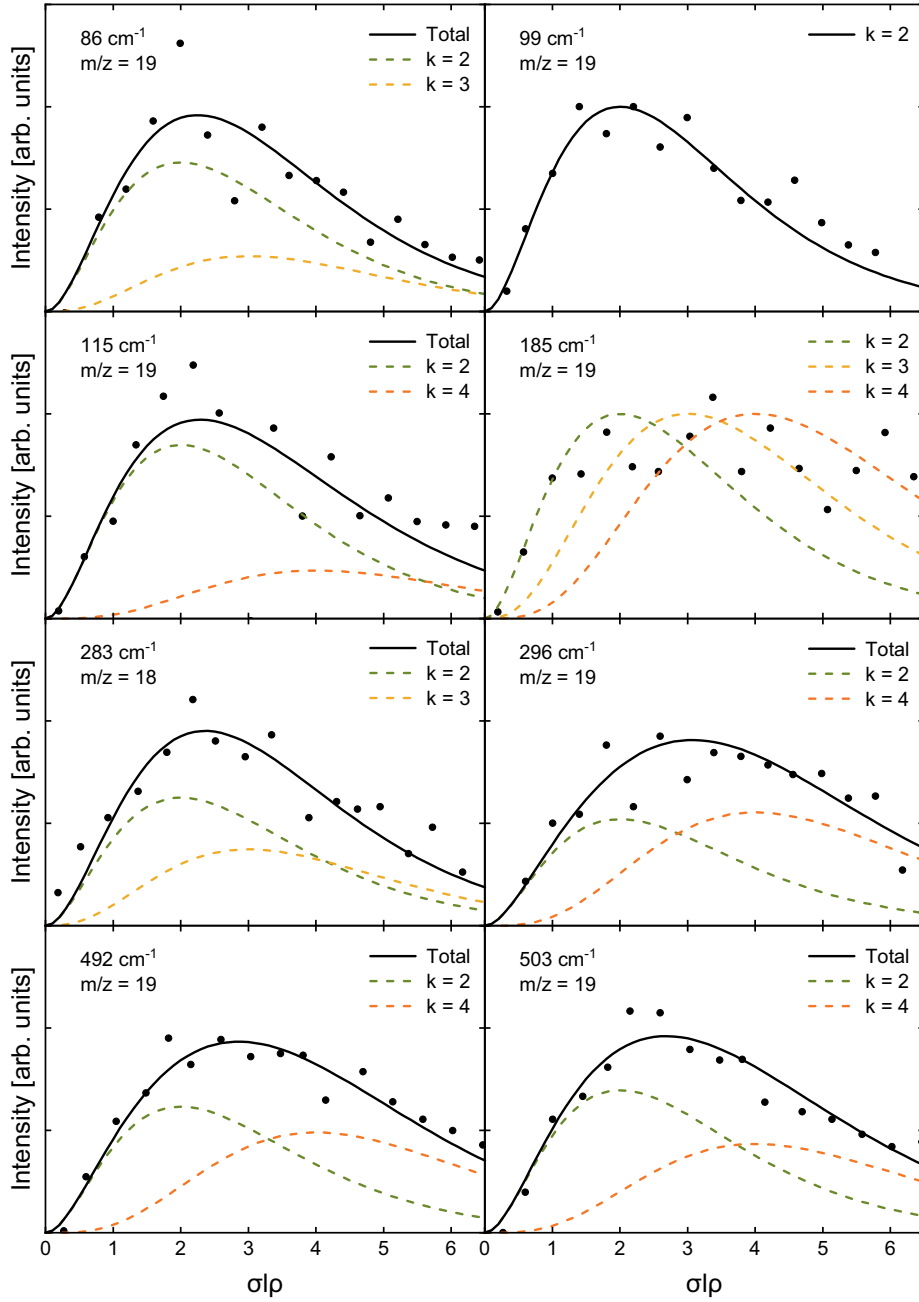
Figure 1: Normalized signal intensities of the signals in the FIR/THz spectrum of water dimer $(H_2O)_2$ as a function of the product $\sigma l \rho$. Each pickup curve was reproduced by Poisson statistics using either a model with a distinct value for k or by a combined model with different values for k_1 and k_2 (black solid lines). For the latter, the contributions of the models with distinct k values are shown as dashed lines.
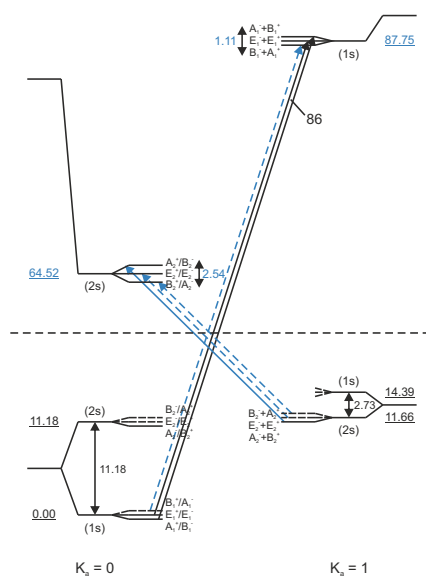
Figure 2: Donor Torsion (DT) VRT energy level diagram. Parallel and perpendicular transitions are shown as vertical and diagonal arrows, respectively; black arrows: observed in the present study and in gas phase studies; blue arrows: only observed in gas phase studies; red arrows: present study only. For bands observed in the present study, the transition frequencies are shown next to the arrows (black and red). Values shown in blue correspond to gas phase data. All frequencies and energies are given in cm^{-1}.
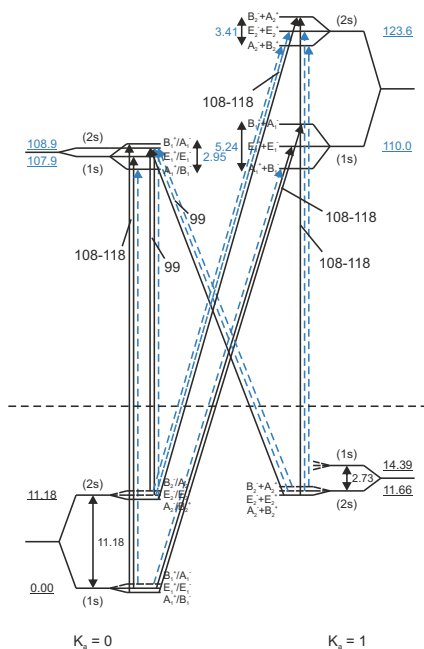
Acceptor Wag

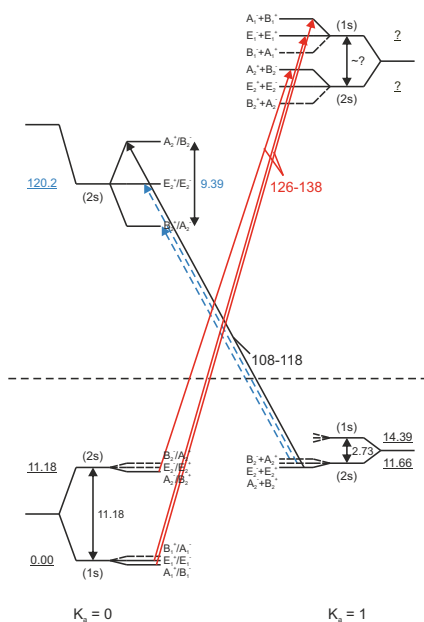Figure 3: Acceptor Wag (AW) VRT energy level diagram.

Acceptor Twist

Figure 4: Acceptor Twist (AT) VRT energy level diagram.

References

[1] D. Mani, T. Fischer, R. Schwan, A. Dey, B. Redlich, A. Van der Meer, G. Schwaab, M. Havenith, *RSC Adv.* **2017**, *7*, 54318–54325.

[2] K. von Haeften, S. Rudolph, I. Simanovski, M. Havenith, R. E. Zillich, K. B. Whaley, *Phys. Rev. B* **2006**, *73*, 054502.

[3] M. Ortlieb, Ö. Birer, M. Letzner, G. Schwaab, M. Havenith, *J. Phys. Chem. A* **2007**, *111*, 12192–12199.

[4] J. P. Toennies, A. F. Vilesov, *Annu. Rev. Phys. Chem.* **1998**, *49*, 1–41.

[5] C. Callegari, K. K. Lehmann, R. Schmied, G. Scoles, *J. Chem. Phys.* **2001**, *115*, 10090–10110.

[6] J. P. Toennies, A. F. Vilesov, *Angew. Chem. Int. Ed.* **2004**, *43*, 2622–2648.

[7] F. Stienkemeier, K. K. Lehmann, *J. Phys. B* **2006**, *39*, R127.

[8] M. Choi, G. Douberly, T. Falconer, W. Lewis, C. Lindsay, J. Merritt, P. Stiles, R. Miller, *Int. Rev. Phys. Chem.* **2006**, *25*, 15–75.

[9] D. Oepts, A. Van der Meer, P. Van Amersfoort, *Infrared Phys. Technol.* **1995**, *36*, 297–308.

[10] D. Brink, S. Stringari, *Z. Phys. D* **1990**, *15*, 257–263.

[11] C. Leforestier, K. Szalewicz, A. Van Der Avoird, *J. Chem. Phys.* **2012**, *137*, 014305.

[12] Y. Scribano, C. Leforestier, *J. Chem. Phys.* **2007**, *126*, 234301.

[13] Y. Wang, J. M. Bowman, *Chem. Phys. Lett.* **2010**, *491*, 1–10.

[14] G. Brocks, A. Van Der Avoird, B. Sutcliffe, J. Tennyson, *Mol. Phys.* **1983**, *50*, 1025–1043.

[15] T. R. Dyke, *J. Chem. Phys.* **1977**, *66*, 492–497.

[16] C. Lanczos, *An iteration method for the solution of the eigenvalue problem of linear differential and integral operators*, United States Governm. Press Office Los Angeles, CA, **1950**.

[17] R. E. Wyatt, D. S. Scott in *North-Holland Mathematics Studies, Vol. 127*, Elsevier, **1986**, pp. 67–79.

[18] W. L. Hase, *Classical trajectory simulations: Initial conditions, Vol. 1*, Wiley, New York, **1998**, pp. 402–407.

[19] Y. Wang, X. Huang, B. C. Shepler, B. J. Braams, J. M. Bowman, *J. Chem. Phys.* **2011**, *134*, 094509.

[20] H. Partridge, D. W. Schwenke, *J. Chem. Phys.* **1997**, *106*, 4618–4639.

[21] A. Shank, Y. Wang, A. Kaledin, B. J. Braams, J. M. Bowman, *J. Chem. Phys.* **2009**, *130*, 144314.

[22] L. Lodi, J. Tennyson, O. L. Polyansky, *J. Chem. Phys.* **2011**, *135*, 034113.

[23] H. Liu, Y. Wang, J. M. Bowman, *J. Chem. Phys.* **2015**, *142*, 194502.

[24] H. Liu, Y. Wang, J. M. Bowman, *J. Phys. Chem. B* **2016**, *120*, 1735–1742.